EPJ Applied Metamaterials

RESEARCH ARTICLE

OPEN ACCESS

Riemann–Hilbert technique scattering analysis of metamaterial-based asymmetric 2D open resonators

Piotr M. Kamiński[1,*], Richard W. Ziolkowski[2,3], and Samel Arslanagić[1]

[1] Department of Electrical Engineering Technical, University of Denmark, Kgs. Lyngby 2800, Denmark
[2] Department of Electrical and Computer Engineering, University of Arizona, Tucson, 85721-0104, USA
[3] Global Big Data Technologies Centre, University of Technology Sydney, Ultimo, NSW 2007, Australia

Abstract. The scattering properties of metamaterial-based asymmetric two-dimensional open resonators excited by an electric line source are investigated analytically. The resonators are, in general, composed of two infinite and concentric cylindrical layers covered with an infinitely thin, perfect conducting shell that has an infinite axial aperture. The line source is oriented parallel to the cylinder axis. An exact analytical solution of this problem is derived. It is based on the dual-series approach and its transformation to the equivalent Riemann–Hilbert problem. Asymmetric metamaterial-based configurations are found to lead simultaneously to large enhancements of the radiated power and to highly steerable Huygens-like directivity patterns; properties not attainable with the corresponding structurally symmetric resonators. The presented open resonator designs are thus interesting candidates for many scientific and engineering applications where enhanced directional near- and far-field responses, tailored with beam shaping and steering capabilities, are highly desired.

Keywords: Asymmetric resonators / Line source / Metamaterials / Riemann–Hilbert techniques / Scattering

1 Introduction

One of the successful outcomes of metamaterial (MTM) research efforts has been the realization of the fact that a proper combination of double-positive (DPS) with single-negative (SNG) or double-negative (DNG) materials can provide highly resonant, electrically small scattering and radiating structures [1–5]. Particular attention, in most cases, has been devoted to *symmetric* two-dimensional (2D) cylindrical and three-dimensional (3D) spherical MTM-based structures. The adjective "symmetric" refers here to the structural symmetry in the constituent materials and layers of the structure, and not to the location of possible exciting discrete sources. The latter are asymmetrically located with respect to the material structure in most of the studied cases. It has been shown analytically that such electrically small structures can lead to large enhancements of the power radiated by nearby sources. This behavior, when the structures include gain, has been described as being super-resonant [6]. For symmetric 2D circular MTM-based structures excited by nearby line sources, strong dipole and quadrupole mode responses have been demonstrated [3]. The strength of these responses was found to be modified by simply altering the location of the exciting source. This

agility provides a means to tailor, to some extent, the directivity of such configurations. Similar concepts have been exploited in the optical domain to tailor the directivity of related electrically small passive [4] and active coated nano-particles [7].

Due to their promising potential in applications of societal importance, intense attention has been devoted recently to the growing field of optical antennas or nanoantennas and sensors (see, e.g., [8,9], and the works referenced therein). Much attention has been devoted to enhancing and steering the directivity of nanoantennas [10,11] by, e.g., introducing perforations in the constituent material layers. In such *asymmetric* designs, the asymmetry leads to the excitation of higher order modes (HOMs) which are required to enhance the directivity. Moreover, breaking the symmetry in similar plasmonic nanostructures has been found to lead to other interesting optical scattering properties [12,13].

Inspired by these recent directivity enhancement efforts in the optical domain [10,11], it is of interest to examine if a similar approach can be exploited to enhance the directivity of the 2D MTM-based coated core–shell structures described analytically in [3] by making them asymmetric. To this end, we investigate resonant scattering from passive 2D MTM-based core–shell structures covered by an infinitely thin and perfectly electrically conducting (PEC) cylindrical shell that has an infinite axial

* e-mail: pmarka@elektro.dtu.dk

slot. The presence of this slot (or aperture), whose transverse extent is arbitrary, makes the resultant configuration asymmetric. The structure is excited by a nearby infinitely long electric line source (ELS) oriented parallel to the cylinders axes. These open resonators are examined for their potential to achieve enhanced and controllable directivities through pattern shaping and steering capabilities. This scattering problem is studied analytically by the so-called dual-series approach and its reformulation in terms of the equivalent Riemann–Hilbert problem known from the theory of complex variables [14]. The analytical solution provides an efficient determination of the resulting fields, and a number of derived quantities, e.g., the radiated power and directivity. Particular attention will be devoted to the influence of the aperture extent and the ELS location on the resonant properties of these resonators. Theoretical designs with large radiated powers and partially steerable Huygens-like directivities will be presented. The influence of loss and dispersion, inevitably present in any MTM, will also be taken into account. Moreover, a frequency dispersive gain model is introduced in some configurations, making them active. It is then shown that gain can, not only overcome the MTM losses, but even more significantly amplify the response of the studied configurations. The studied asymmetric MTM-based open resonator theoretical designs may serve as potential candidates for a variety of scientific and engineering applications where enhanced directional near- and far-field responses, along with notable beam shaping and steering capabilities, are desired.

In its context as the analytical solution of related canonical scattering problems, the present work is a natural extension of the studies in [15–18]. In there, the plane wave scattering from and coupling to an infinite metallic circular cylinder with an infinite axial aperture enclosing concentric dielectric and metallic cylinders was studied analytically as a dual-series problem and solved with Riemann–Hilbert techniques. Related studies were also conducted in the Russian literature (see, e.g., [19,20]).

This article is organized as follows. Section 2 introduces the configuration, and describes the steps behind the analytical solution. Specifically, the dual-series representation of the problem is derived, and is cast into the equivalent Riemann–Hilbert problem. Derived quantities, used to study the performance of the investigated configurations, are also introduced. Section 3 includes the numerical results for a variety of asymmetric MTM-based configurations. Section 4 provides a summary and conclusions from this work. Throughout the manuscript, the engineering time factor $\exp(j\omega t)$, with ω being the angular frequency and t being the time, is assumed and suppressed.

2 Open resonator scattering problem and its solution

The scattering problem of a line source excitation of a 2D open resonator loaded with concentric MTM layers is introduced. This dual-series problem is solved analytically with a Riemann–Hilbert technique. Related analytically-obtained performance characteristics are introduced.
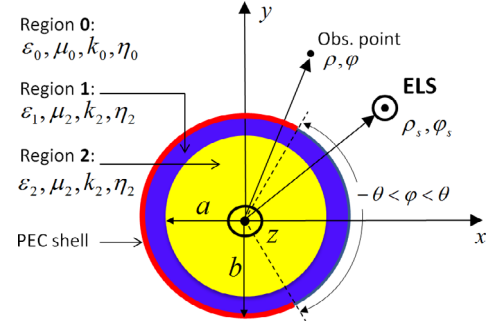

Fig. 1. The cross-sectional view of the 2D open resonator scattering problem under investigation and the parameters defining this configuration.

2.1 Configuration

The cross section of the asymmetric configuration under investigation is shown in Figure 1.

It consists of a circular cylindrical core (region 2) of radius a covered concentrically with a cylindrical shell (region 1) of outer radius b. An infinitely thin concentric PEC shell of radius b with an aperture of angular extent 2θ covers the core–shell system. The host medium is free-space (region 0) with permittivity ε_0, permeability μ_0, and, thus, wave number $k_0 = \omega\sqrt{\varepsilon_0\mu_0}$ and intrinsic wave impedance $\eta_0 = \sqrt{\mu_0/\varepsilon_0}$. Region i, $i = 1, 2$, has the permittivity ε_i, permeability μ_i; their wave number and intrinsic wave impedance are, respectively, given by $k_i = \omega\sqrt{\varepsilon_i\mu_i}$ and $\eta_i = \sqrt{\mu_i/\varepsilon_i}$. The structure is excited by an infinitely long ELS, which is driven with a constant current I_e [A]. The ELS is oriented parallel to the axis of the cylinders. A cylindrical coordinate system (ρ, φ, z) and the associated Cartesian coordinate system (x, y, z) are introduced such that the z-axis of both coincides with the axis of the cylinders. The location of the ELS is denoted by (ρ_s, φ_s), and the location of the observation point is denoted by (ρ, φ). The extent of the aperture is defined symmetrically about the x-axis as $-\theta < \varphi < \theta$.

2.2 Field expansions and dual-series formulation

For discussion purposes only, the ELS is assumed to be located inside region 2. The known electric field radiated by the ELS is expanded in cylindrical waves as [21]

$$\boldsymbol{E}_{\mathrm{ELS}} = -\hat{z}\,\frac{I_e k_2 \eta_2}{4}\sum_{m=-\infty}^{\infty} d_{|m|}e^{jm(\varphi-\varphi_s)}, \quad (1a)$$

with

$$d_{|m|} = \begin{cases} J_{|m|}(k_2\rho)H_{|m|}^{(2)}(k_2\rho_s), & \rho \le \rho_s, \\ J_{|m|}(k_2\rho)H_{|m|}^{(2)}(k_2\rho_s), & \rho \ge \rho_s, \end{cases} \quad (1b)$$

where $J_{|m|}(\cdot)$ is the Bessel function of order m, and $H_{|m|}^{(2)}(\cdot)$ is the Hankel function of the second kind and order m. We note that the same approach applies, of course, for other ELS locations. However, while straightforward to obtain, the functional forms of a number of quantities entering into the resulting dual-series equations will differ from the

presently derived ones when the ELS is in either region 0 or region 1. The corresponding unknown scattered electric fields, denoted by $\boldsymbol{E}_i$, with $i = 0$, 1, and 2 designating, respectively, regions 0, 1, and 2, are expanded similarly [21]

$$\boldsymbol{E}_2 = -\hat{z}\frac{I_e k_2 \eta_2}{4} \sum_{m=-\infty}^{\infty} A_m J_{|m|}(k_2 \rho)e^{jm\varphi}, \tag{2a}$$

$$\boldsymbol{E}_1 = -\hat{z}\frac{I_e k_1 \eta_1}{4} \sum_{m=-\infty}^{\infty} \left[B_m J_{|m|}(k_1 \rho) + C_m H_{|m|}^{(2)}(k_1 \rho) \right]e^{jm\varphi}, \tag{2b}$$

$$\boldsymbol{E}_0 = -\hat{z}\frac{I_e k_0 \eta_0}{4} \sum_{m=-\infty}^{\infty} D_m H_{|m|}^{(2)}(k_0 \rho)e^{jm\varphi}, \tag{2c}$$

where the quantities A_m, B_m, C_m, and D_m are the unknown expansion coefficients. The magnetic fields corresponding to (1) and (2) follow at once from the Maxwell–Faraday law, and are not included for brevity. In order to determine the unknown coefficients, the boundary conditions are applied in the following order. The continuity of the tangential components of the total electric and magnetic fields is first imposed at the boundary $\rho = a$. The continuity of the tangential component of the total electric fields is then imposed at the boundary $\rho = b$. This reduces the total number of expansion coefficients needed to represent the scattered fields to a single expansion coefficient, e.g., B_m. Finally, two boundary conditions are imposed at the boundary $\rho = b$: the tangential components of the total electric field must be zero on the PEC shell, and the tangential components of the total magnetic field must be continuous across the aperture. With the application of these conditions, the problem is reduced to the following dual-series equations:

$$\sum_{m=-\infty}^{\infty} g_m e^{jm\varphi}, \quad |\varphi| > \theta, \tag{3a}$$

$$\sum_{m=-\infty}^{\infty} g_m \tau_m e^{jm\varphi} = f(\varphi), \quad |\varphi| < \theta, \tag{3b}$$

where the auxiliary coefficients

$$g_m = B_{|m|}\left[J_{|m|}(k_1 b) - \Omega_{|m|} H_{|m|}^{(2)}(k_1 b) \right] + H_{|m|}^{(2)}(k_1 \rho)\Psi_{|m|}, \tag{4a}$$

$$\tau_m = \frac{\left[J'_{|m|}(k_1 b)H_{|m|}^{(2)}(k_0 b) - \frac{\eta_1}{\eta_0}H_{|m|}^{(2)\prime}(k_0 b)J_{|m|}(k_1 b) \right]}{-j\pi H_{|m|}^{(2)}\left[J_{|m|}(k_1 b) - \Omega_{|m|}H_{|m|}^{(2)}(k_1 b) \right]}$$
$$+ \frac{\Omega_{|m|}\left[\frac{\eta_1}{\eta_0}H_{|m|}^{(2)\prime}(k_0 b)H_{|m|}^{(2)}(k_1 b) - H_{|m|}^{(2)\prime}(k_1 b)H_{|m|}^{(2)}(k_0 b) \right]}{-j\pi H_{|m|}^{(2)}(k_0 b)\left[J_{|m|}(k_1 b) - \Omega_{|m|}H_{|m|}^{(2)}(k_1 b) \right]}, \tag{4b}$$

$$f(\varphi) = \sum_{m=-\infty}^{\infty} f_m e^{jm\varphi}, \tag{4c}$$

and where the associated terms

$$f_m = \Psi_{|m|}\tau_m H_{|m|}^{(2)}(k_1 b)$$
$$+ \Psi_{|m|}\frac{\frac{\eta_1}{\eta_0}H_{|m|}^{(2)\prime}(k_0 b)H_{|m|}^{(2)}(k_1 b) - H_{|m|}^{(2)\prime}(k_1 b)H_{|m|}^{(2)}(k_0 b)}{-j\pi H_{|m|}^{(2)}(k_0 b)}, \tag{4d}$$

$$\Omega_{|m|} = \frac{J_{|m|}(k_1 a) - \frac{\eta_2 J_{|m|}(k_2 a)}{\eta_1 J'_{|m|}(k_2 a)}J'_{|m|}(k_2 a)}{H_{|m|}^{(2)}(k_1 a) - \frac{\eta_2 J_{|m|}(k_2 a)}{\eta_1 J'_{|m|}(k_2 a)}H_{|m|}^{(2)\prime}(k_1 a)}, \tag{4e}$$

and finally

$$\Psi_{|m|} = \frac{\frac{2je^{-jm\varphi_s}J_{|m|}(k_2 \rho_s)}{\pi k_2 a J'_{|m|}(k_2 a)}}{\frac{k_1}{k_2}\left[\frac{\eta_1}{\eta_2}H_{|m|}^{(2)}(k_1 a) - \frac{J_{|m|}(k_2 a)}{J'_{|m|}(k_2 a)}H_{|m|}^{(2)\prime}(k_1 a) \right]}. \tag{4f}$$

In these expressions, the prime denotes the derivative with respect to the entire argument. The system of equations (3) and (4) represents a dual-series problem of the same form as those studied for asymmetric canonical scattering problems with plane wave excitations [14–18]. These analytical results, especially with the ELS excitation and with the inner cylinders taken to be MTMs are, to the best of our knowledge, the first of their kind.

2.3 Riemann–Hilbert problem and solution

The general objective of the Riemann–Hilbert problem is to determine a sectionally analytic function x that satisfies a given boundary condition across an open or a closed contour. If the limits of the function, x_+ and x_-, respectively, from the inside and outside of an open segment of a contour satisfy the transition condition $x_+ = gx_- + h$, one has an inhomogeneous Riemann–Hilbert problem [14–18]. The dual-series equations (3) are easily cast into this form. By following [15], we first differentiate (3a) with respect to φ and introduce the quantity $x_m = mg_m$. Subsequently, we introduce the functions

$$x_+ = \sum_{m>0} x_m z^m, \tag{5a}$$

$$x_- = -\sum_{m<0} x_m z^m, \tag{5b}$$

which are analytic on the interior and exterior of the unit circle contour. Substitution of (5) into (3) transforms that dual-series problem into the equivalent Riemann–Hilbert problem [14–18]

$$x_+(e^{j\varphi}) = T(e^{j\varphi})x_-(e^{j\varphi}) + F(e^{j\varphi}), \tag{6}$$

where

$$T(e^{j\varphi}) = \begin{cases} +1, & |\varphi| > \theta, \\ -1, & |\varphi| < \theta, \end{cases} \tag{7a}$$

Table 1. Material parameters of the C1 and C2 configurations.

C	ε_2	μ_2	ε_1	μ_1
1	ε_0	μ_0	$\pm\varepsilon_0$	$\pm 4\mu_0$
2	$-\varepsilon_0$	$-\mu_0$	ε_0	μ_0

is the coefficient of the problem, and

$$F(e^{j\varphi}) = \begin{cases} 0, & |\varphi| > \theta, \\ \gamma g_0 + f(\varphi) - \sum_{m \neq 0} x_m \dfrac{|m|}{m} \chi_m e^{jm\varphi}, & |\varphi| < \theta, \end{cases}$$
(7b)

is the free term of the problem. The functions γ and χ_m in (7b) are related to τ_m from (4b) through the relations: $\tau_m = -\gamma$, $m = 0$; and $\tau_m = |m|(1 + \chi_m)$ for $m \neq 0$.

A general solution to the system of equations (6) and (7) has been described in [14]. It was shown that the problem can be formulated as an infinite linear system of equations which can be solved for the unknown coefficients x_m. The links to the aperture coupling problems, as the one depicted in Figure 1, and the behavior of the results obtained when the system is truncated to a finite number of terms were thoroughly discussed in [14–18]. The main advantage of the Riemann–Hilbert approach over conventional modal analyses of the electromagnetic dual-series problems is that its solution has the singular behavior, which occurs at the edge of the aperture [22], built into it. Thus, the convergence of the result for a finite number of terms is rapid. In essence, it provides the Green's function for the open resonator problem. Consequently, both the line source and plane wave excitations are readily handled with the same approach. Once the x_m coefficients are obtained, the associated terms g_m $(x_m = mg_m)$ are readily calculated, thereby enabling the determination of the expansion coefficients, B_m, and, hence, all of the remaining expansion coefficients. With all of these expansion coefficients at hand, the fields are known in all of the regions of interest. This, in turn, allows us to determine several derived quantities and, hence, to quantify the performance of the scattering configurations being studied.

2.4 Derived quantities

Following previous studies [3,7], the configurations at hand will, apart from their field distributions, be examined with regard to their near-field power flow densities, as well as their far-field performance characteristics. The features of the total radiated power will be taken into account through the power ratio (PR). It is defined as the total power radiated by the ELS in the presence of the asymmetric configuration normalized by the total radiated power of the ELS alone in free space. It is the same as the Purcell factor [8]. For the cases studied herein, the PR (in dB) takes the following form:

$$\text{PR} = 10 log_{10}||D_0|^2 + 2 \sum_{m=1}^{\infty} |D_m D_{-m}||, \quad (8)$$

where D_m is the expansion coefficient of the field outside of the structure. The directivity is defined as the radiation intensity in a given direction over the average radiation intensity. Thus, it takes on the following form:

$$D(\varphi) = \frac{|\sum_{m=-\infty}^{\infty} D_m j^{|m|} e^{jm\varphi}|^2}{|D_0|^2 + 2 \sum_{m=1}^{\infty} |D_m D_{-m}|}. \quad (9)$$

Finally, the power flow density for this time harmonic problem is determined from the time averaged Poynting vector: $\boldsymbol{S} = \text{Re}\{\boldsymbol{E} \times \boldsymbol{H}^*\}/2$. The vector field quantities $\boldsymbol{E}$ and $\boldsymbol{H}$ denote the total electric and magnetic fields, respectively, in a given region.

The analytical solution was implemented in MATLAB. This developed code was validated extensively through comparisons with analytical results obtained directly from the formulas and those obtained from related canonical problems, as well as with the corresponding numerical results generated with COMSOL Multiphysics, version 5.0 [23]. Very good agreement is found in all cases between the analytical and numerical results. These validation efforts, together with detailed explanations of any minor and insignificant discrepancies, are summarized in Appendix A.

3 Results and discussion

We focus on two specific, and initially lossless, configurations to convey our general findings in several comparative studies. One employs a DPS material in the core and either a DPS or DNG material in the shell. The other has a DNG material in the core and the complementary DPS material in the shell. In particular, the first configuration (C1) consists of a free-space core layered with either a DPS shell ($\varepsilon_1 = +\varepsilon_0$, $\mu_1 = +4\mu_0$) or a DNG shell ($\varepsilon_1 = -\varepsilon_0$, $\mu_1 = -4\mu_0$). The second configuration (C2) is composed of a DNG core with ($\varepsilon_1 = -\varepsilon_0$, $\mu_1 = -\mu_0$) covered with a free-space shell. These specific material parameters for these two configurations are summarized in Table 1. Again, the structures are excited in all cases by an ELS which is driven with a constant current of 1 [A]; moreover, its frequency is arbitrarily set to 300 MHz.

3.1 Configuration C1

The core–shell part of the C1 configuration, i.e., the problem with the PEC shell absent, was studied thoroughly in [3] and provides a baseline for comparisons with the shell being present. It was demonstrated that the core–shell geometry exhibited strong resonant dipole and quadrupole mode responses. There were also significant enhancements of the power radiated by the ELS alone that were
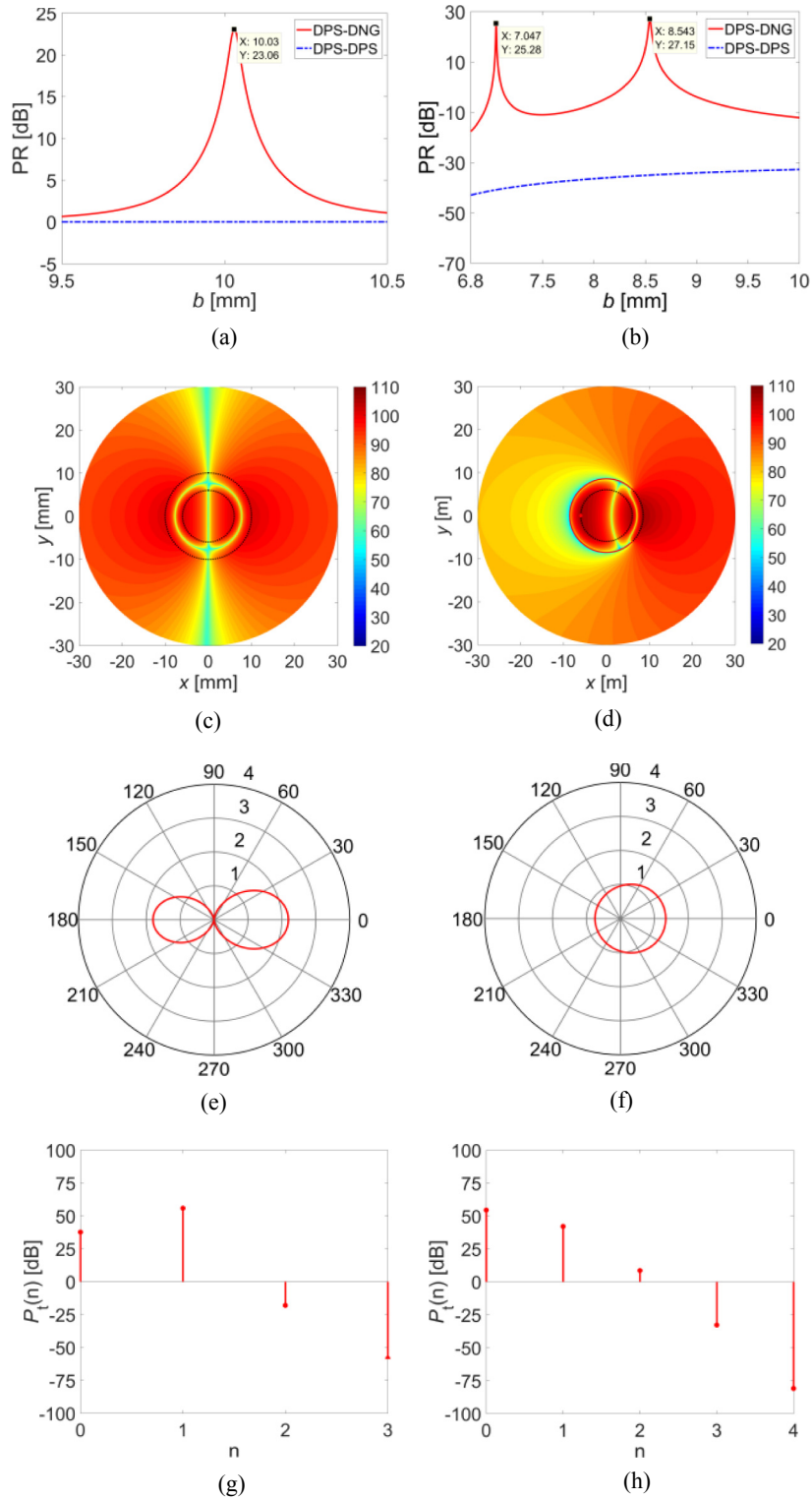
Fig. 2. The C1 configuration results in (a) and (b) show the power ratio (PR) as a function of the outer radius b; (c) and (d) show the electric field magnitude resulting in the peak PR values in (a) and (b), respectively; (e) and (f) show the associated directivities, while (g) and (h) show the associated power spectrums. The left column, i.e., (a), (c), (e) and (g), corresponds to the case with no PEC shell. The right column corresponds to the case with the PEC shell having an aperture extent of $2\theta = 90°$. Figure 2d, f and h corresponds to the second peak PR value attained for $b = 8.543$ mm.

Fig. 3. The electric field magnitude (dB) (a) and the power spectrum (b) for the C1 configuration with the PEC shell having an aperture extent of $2\theta = 90°$. These results correspond to the first peak PR value in Figure 2b attained for $b = 7.047$ mm.

associated with these resonances. It is therefore of interest to assess the impact of the open PEC shell on these outcomes.

To this end, we set the radius of the free-space core to $a = 6$ mm and locate the ELS in this region along the negative x-axis at $\rho_s = 5.99$ mm. The outer radius b of the DPS/DNG shell (and equivalently the radius of the PEC shell) is varied to find its value which produces the peak enhancement of the PR. As shown in [3] and summarized below for ease of comparison, the PR of the DNG-based configuration C1 in the absence of the PEC shell shown in Figure 2a is significantly enhanced (PR ≈ 23 dB) at $b = 10.03$ mm. The corresponding DPS-based configuration yields no PR enhancement of the ELS because the structure size is electrically small and, as a consequence, kb is well below any of its natural resonance values. As the overall power spectrum (i.e., the power in each given mode m) shown in Figure 2g indicates, the peak PR value is due to the resonant excitation of a dominant dipole mode inside the structure. This is also clear from Figure 2c where an almost symmetric (with respect to the x- and y-axes) dipole pattern is found for the electric near-field magnitude distribution (dB scale). More specifically, Figure 2c shows the quantity: $20\log_{10}|\boldsymbol{E}/1\,[\mathrm{V/m}]|$. The associated directivity pattern is found in Figure 2e and is seen to be slightly asymmetric with respect to the y-axis. Figure 2g also emphasizes the fact that very little of the total radiated power is contained in any of the HOMs.

The PEC shell is then introduced into the same configuration C1 with an aperture extent of $2\theta = 90°$. The location of the ELS remains unchanged. The resulting PR values are shown in Figure 2b as functions of the outer radius b for both the DPS and DNG interior shell layers. Again, because of its electrically small nature, the DPS case does not lead to any enhancements of the PR. In fact, because the structure captures and stores some of power radiated by the ELS, the PR values are significantly decreased; i.e., the ELS alone radiates more power into the far field in free space than in the presence of the open structure. On the other hand, for the DNG shell case, resonant behavior is clearly evident in the PR values. There are two resonances for $b = 7.047$ and 8.543 mm; the peak PR values for those values are 25.28 and 27.15 dB, respectively. These peak PR values are comparable to the one associated with the bare configuration (the open

PEC shell being absent). However, notice that the presence of the PEC shell decreases the outer radius b for which the PR maxima are attained.

As can be seen in Figure 2d, the electric field distribution associated with the PR peak at $b = 8.543$ mm is primarily dipolar in the interior of the open shell, but is a mixture of several modes in its exterior. The edge singularities of the aperture facilitate the coupling of the incident field to an infinite number of modes. The strengths of this coupling depend on the interior and exterior environment of the open resonator. This is further confirmed by the power spectrum shown in Figure 2h. The monopole and dipole modes are almost equally excited, but one finds that the HOMs are excited more than in the absence of the PEC shell. Furthermore, notice that the near-field distribution is quite asymmetric with respect to the y-axis. The open PEC shell appears to be channeling the scattered power away from the ELS and out of the aperture. On the other hand, as one would expect, the near-field distribution is very symmetric with respect to the x-axis. Thus, the presence of the open shell produces very directive near-field beams even for this electrically small structure in agreement with the reported 3D cases [10,11]. However, despite the increased presence of the HOMs for the open PEC shell case, their impact does not extend into the far-field. There is only a small increase of the (far-field) directivity along the x-axis as illustrated by comparing the results in Figure 2e and f. Notice from Figure 2g and h that the monopole mode is more strongly excited in the open PEC case. This explains the differences in the shapes of these directivity patterns.

Before explaining the physics behind the results in Figure 2, we note that a PR peak in Figure 2b is also attained for $b = 7.047$ mm. It corresponds primarily to a quadrupole mode inside of the shell, and a mixture of modes outside of it. This is clear from Figure 3a which shows the resulting electric near-field distribution. Figure 3b, which depicts the resulting power spectrum, indicates that the mixture of the modes in the far-field is basically the same as that of the resonance at $b = 8.543$ mm. Consequently, its directivity pattern resembles the one shown in Figure 2f and, therefore, has not been included here.

As noted above, the presence of the open PEC shell decreases the required value of the outer radius b for the DNG shell case as compared to the case with no PEC shell.
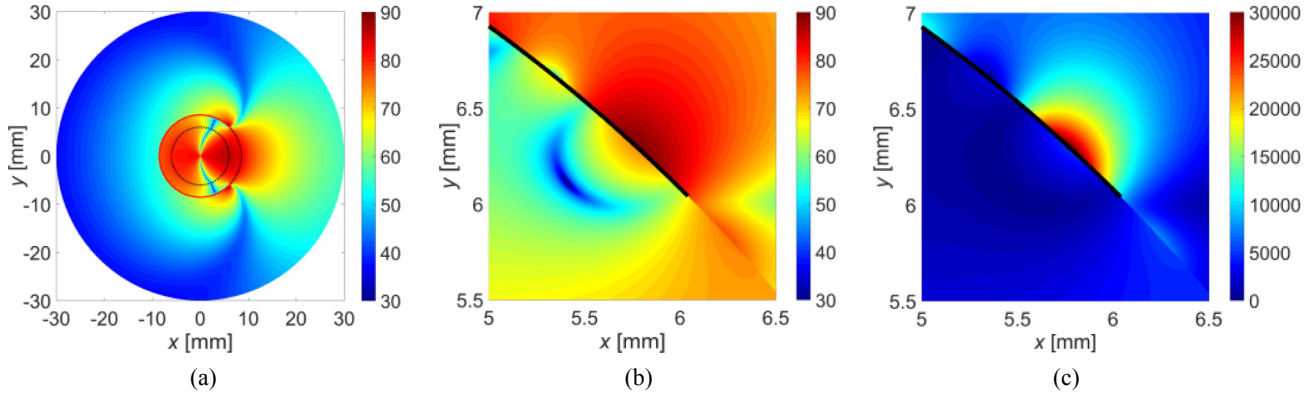
Fig. 4. Magnetic field results for the C1 configuration with $b = 8.543$ mm that corresponds to the second resonant peak PR value in Figure 2b. (a) Distribution of its magnitude (dB), and zoom-ins near the upper edge of the aperture of the open PEC shell in (b) dB, and in (c) linear scale.
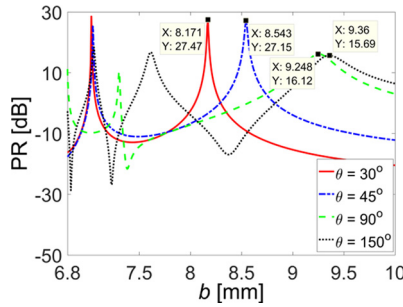

Fig. 5. The PR as a function of the outer radius b for the DNG-based configuration C1 with several different aperture extents: 2θ.

Fig. 6. The PR values as functions of the outer radius b for configuration C2 for varying aperture extent: 2θ.

With the ELS parallel to edges of the aperture of the open PEC shell, it is the scattered magnetic fields that take on the singular behavior [22]. They acquire a square root singularity as the distance from the edge goes to zero, whereas the electric fields go to zero there. Thus, the ELS and the open shell produce inductance. On the other hand, these strong magnetic fields interact directly with the MNG components of the DNG material yielding a strong capacitance. The gap of the open shell also provides more capacitance. Hence, the system acts as an LC-resonator. The strong capacitive contributions lower the amount of the DNG material needed to achieve the resonance and, hence, the radius b is smaller (the thickness of the DNG material is less) than without the open shell being present. The behavior of the magnetic field, $\boldsymbol{H}$, for the $b = 8.543$ mm C1 configuration, which corresponds to the right column of Figure 2, is illustrated in Figure 4. The distribution of the quantity $20\log_{10}|\boldsymbol{H}/1 \ [\text{A/m}]|$ is shown in Figure 4a. A zoom-in of these values (dB) near the upper edge of the open PEC shell is given in Figure 4b. One can clearly see the large values of the magnetic field near it arising from the edge singularity. A further zoom-in (linear, not log scale) of the magnetic field distribution near that upper edge is given in Figure 4c; it very clearly illustrates this singular behavior. Again, it is the presence of these edge singularities in the electromagnetic field that facilitates the coupling of the ELS field to the HOMs of the open composite structure. Note that the singularity appears to be located slightly away from the edge in Figure 4c. As discussed in the appendix, this is a consequence of the software being able to handle only a finite
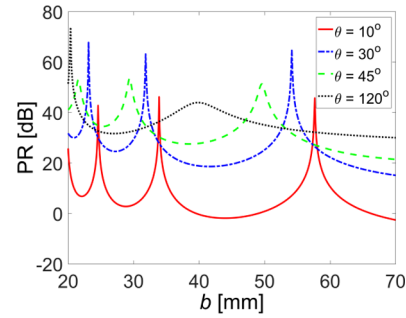
number of modes/terms in the series (the software environment crashes if more than 50 (60) modes are used for the C1 (C2) configuration). As more terms are included in the sum, this Gibbs-like behavior vanishes.

The corresponding PR values for scans of the outer radius b for the C1 configurations with different aperture extents, i.e., for $2\theta = 60°, 90°, 180°$, and $300°$, are shown in Figure 5. The resonances attained for $b > 8$ mm all correspond to a dipole mode inside the PEC shell, while those attained for smaller radii values correspond to the presence of HOMs, as noted in Figure 3 for the quadrupole mode. As the aperture size increases, i.e., as the extent of the PEC shell decreases, a larger outer radius b is needed to attain the resonance for a given mode (e.g., for the dipole mode). This behavior is expected since an increasing aperture extent 2θ means that the configuration is approaching the one with no PEC shell. Thus, the value of b converges gradually to the value 10.03 mm as the aperture extent increases. Similarly, an increasing aperture (or larger gap) lowers the effective capacitance associated with it. Thus, more DNG material is needed to achieve the LC resonance, and hence, is obtained by increasing its thickness (larger b).

3.2 Configuration C2

The configuration C2, which is composed of a DNG core layered with a free-space shell, was also studied. This core–shell configuration is again covered with an open PEC shell. As before, we set the radius of the DNG core to $a = 6$ mm.
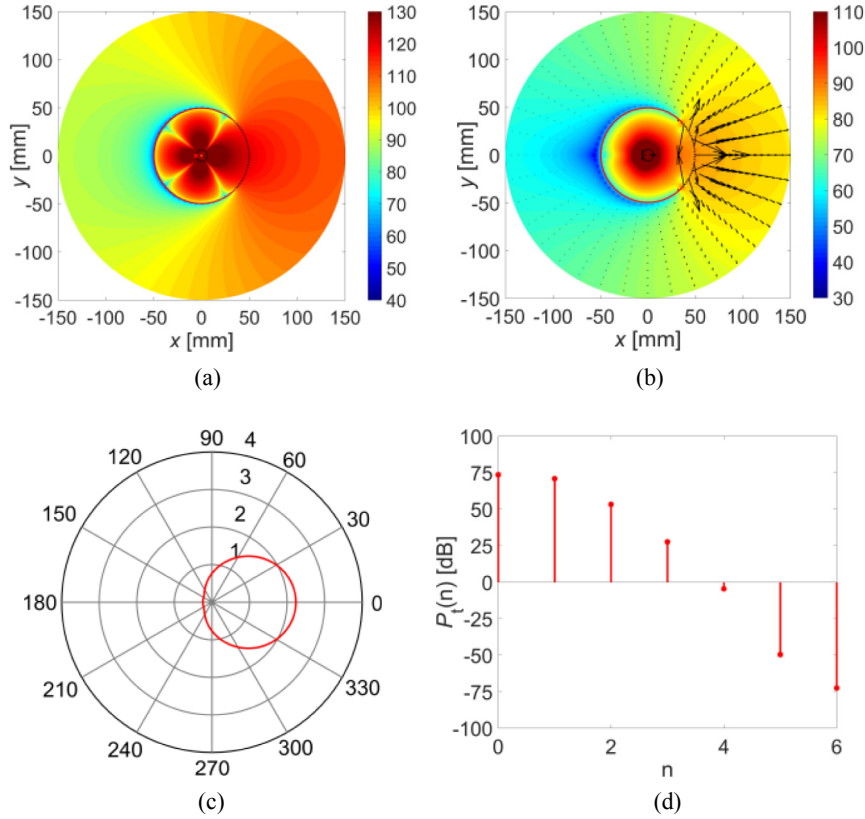
Fig. 7. The magnitude of the electric field (dB) (a), the vector power density (b), the directivity (c) and the overall power spectrum (d) for the configuration C2 with an aperture extent of $2\theta = 90°$ and the outer shell radius $b = 49.6$ mm. This case corresponds to the right-most PR resonance in Figure 6 attained for $\theta = 45°$.

Moreover, unless otherwise stated, the ELS is located inside this DNG core along the negative x-axis at $\rho_s = 5.99$ mm. Figure 6 shows the PR values as a function of the outer radius b of the free-space shell and, hence, the radius of the PEC shell for varying aperture extents: $2\theta = 20°$, $60°$, $90°$, and $240°$.

Because the DNG material is now far from the edges of the aperture and is fixed in size, one finds the LC resonances occurring for significantly larger shells than observed for the DNG C1 configuration shown in Figure 3. The resonances attained for $b > 35$ mm all correspond to a quadrupole mode inside the PEC shell, while those attained for lower radii values again correspond to HOMs. No dipole resonances were in evidence for this configuration for the illustrated range of the outer radius values b and even beyond it. Also in direct contrast to the DNG C1 configuration results, the outer radius b needed to attain a given resonance for this C2 configuration decreases as the aperture extent increases. This occurs because the DNG material is now in the core where the electric field level is the largest. Thus, the inductive contribution is large as these electric fields interact with the ENG components of the DNG core. As the aperture extent increases, smaller b values are needed to continue the concentration of the electric fields in the core and maintain the LC resonance. Furthermore, as Figure 6 illustrates, the resonances are broader for the larger aperture extents because the fields are less confined in the interior and, hence, the loss to radiation in these very open resonators is larger.

The near- and far-field properties of the C2 configuration reveal more features. To illustrate them, Figure 7 shows the particular case where the aperture extent is $2\theta = 90°$ and $b = 49.6$ mm. This configuration corresponds to the right-most PR resonance in Figure 6 for $\theta = 45°$. The corresponding magnitude of the electric field distribution (dB) and the vector power density distribution (i.e., the distribution of the quantity $10\log_{10}|\mathbf{S}/1\,[\text{W/m}^2]|$ in color and $\mathbf{S}$ in vector format); the directivity; and the overall radiated power spectrum are shown in Figure 7. Figure 7a shows that the electric field in the interior of the open PEC shell is primarily of quadrupole form and is concentrated in the DNG core. Figure 7b shows that most of the scattered power has been radiated in the $x > 0$ half-space. This behavior is very pronounced in the vicinity of the aperture and is further evidenced by the very strong flow of the vector power density into the $\varphi = 0°$, direction, along the $+x$-axis. As shown in Figure 7c, the maximum directivity is attained in this direction and is slightly larger than 2, while the front-to-back ratio (i.e., $|\mathbf{E}(\varphi = 0°)|/|\mathbf{E}(\varphi = 180°)|$, with the fields evaluated in the far-field) is quite large: FTBR $= 3.03 = 9.64$ dB.

Consequently, this C2 configuration produces a significant enhancement of the directivity along the $+x$-axis and outperforms any of the studied C1 configurations in this regard. This far-field response is a direct outcome of the presence of several HOMs in the overall power spectrum as shown in Figure 7d. Clearly, there is a strong
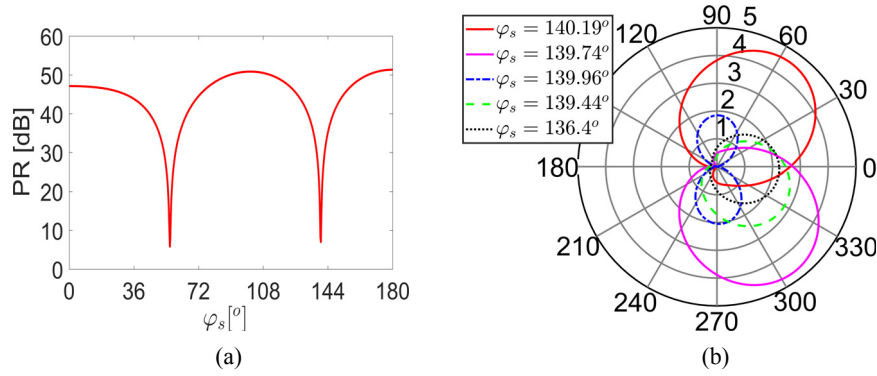
Fig. 8. (a) The PR as a function of φ_s, i.e., the angular ELS location for the structure in Figure 7. (b) The associated directivities for ELS locations close to the second minimum found in (a).

combination due to the excitation of several HOMs, including the monopole ($m = 0$), dipole ($m = 1$), quadrupole ($m = 2$), and sextupole ($m = 3$) modes. Thus, because the edges of the aperture are surrounded only by free space, the coupling to the associated HOMs is much stronger and, hence, the C2 configuration leads to a notably stronger excitation of HOMs than any of the C1 configurations.

As a consequence of this strong HOM generation, the impact of different angular positions of the ELS on the scattering properties of the configuration C2 was also studied. With the source distance fixed at $\rho_s = 5.99$ mm, Figure 8a shows the PR values as a function of the angular position φ_s of the ELS. Owing to the strong excitation of the quadrupole mode inside the PEC shell, the PR attains its largest values when the ELS is located at the points where the largest field magnitudes are attained, i.e., for $\varphi_s = 0°$, $90°$, $180°$, and $270°$ (not shown). Due to the same reasons, the PR exhibits very distinct minima at φ_s where the fields interior to the PEC shell are very low. The directivities associated with the local maxima in Figure 8a are basically dipolar with the peak maximum values occurring along the $\varphi_s \approx 90°$ and $270°$ directions.

On the other hand, because of the presence of several HOMs, interesting Huygens-like directivities result for ELS locations just before and after those giving the local minimum PR values. For example, in the case of the second minimum in Figure 8a, attained at $\varphi_s = 139.96°$, very enhanced and steerable Huygens-like patterns with a directivity of 4.58 ($=6.61$ dB) and a large FTBR value, 22.86 ($=27.18$ dB), respectively, are attained when the ELS is located symmetrically with respect to the minimum at $\varphi_s = 139.74°$ (before it) and at $\varphi_s = 140.19°$ (after it), see Figure 8b. Thus, a very small change in the angular position of the ELS can lead to a profound change in both the value of the maximum directivity and the direction in which it is attained. It is worth noting in contrast that a change in the angular position of the ELS when the open PEC shell is not present leads to a mere rotation of a dipolar pattern. This behavior confirms that the enhanced Huygens-like patterns observed for the C2 configuration are a direct result of the presence of the open PEC shell and the subsequent excitation of its HOMs.

An obvious drawback of the results reported in Figure 8b is the low peak value of the radiated power. The resulting peak PR value is only 8.23 dB. In order to design a configuration exhibiting enhanced and steerable directivities

accompanied with very large values of the radiated power, several C2 configurations with larger aperture extents were considered. In these cases, the dark resonances (minima in the PR values) were found to be wider and shallower (the latter referring to the fact that the difference between maximum and minimum PR values were not found to be nearly as profound as was the case reported in Figure 8a). This allowed the possibility of beam steering without any significant decrease of the peak PR values.

More specifically, the outer radius b was swept for various combinations of the angular ELS location φ_s and the aperture extent 2θ. Figure 9a shows the electric field magnitude when the ELS is at $\varphi_s = 103.33°$, the aperture extent $2\theta = 180°$, and the outer radius $b = 41.74$ mm. Figure 9b shows the corresponding directivity pattern. The minimum PR value is 36.64 dB. The patterns are Huygens-like, with a maximum directivity of 3.52 ($=5.46$ dB) in the main scattering direction $\varphi = 64.00°$. There is essentially no back-lobe, giving a very large FTBR $= 39.16$ ($=31.86$ dB). Note that the back-lobe achieves its minimum when the ELS is located near the aperture edge just inside the PEC shell. The main beam direction in Figure 9 can be partially steered by slight variations of the ELS angular position near the PR minimum value. Since the PR minimum value is 36.64 dB (which is merely 11 dB below the maximum PR value), highly steerable Huygens-like directivities (with a maximum value of $3.52 = 5.46$ dB) can be obtained from these electrically small structures through slight angular displacements of the ELS locations around the PR minimum location while simultaneously retaining rather impressive PR levels.

3.3 Dispersion and loss effects for configuration C2

In our initial discussion, the materials in the C2 configuration were taken to be lossless and nondispersive. Since realistic DNG materials are both lossy and dispersive, the influence of these effects must be assessed. To this end, the well-known Lorentz dispersion model of both the permittivity and permeability of the DNG core was used. The model is given by

$$\zeta(\omega) = \zeta_0 \left(1 - \frac{\omega_{p\zeta}^2}{\omega^2 - j\Gamma_\zeta \omega - \omega_{r\zeta}^2} \right) = \zeta'(\omega) - j\zeta''(\omega), \quad (10)$$
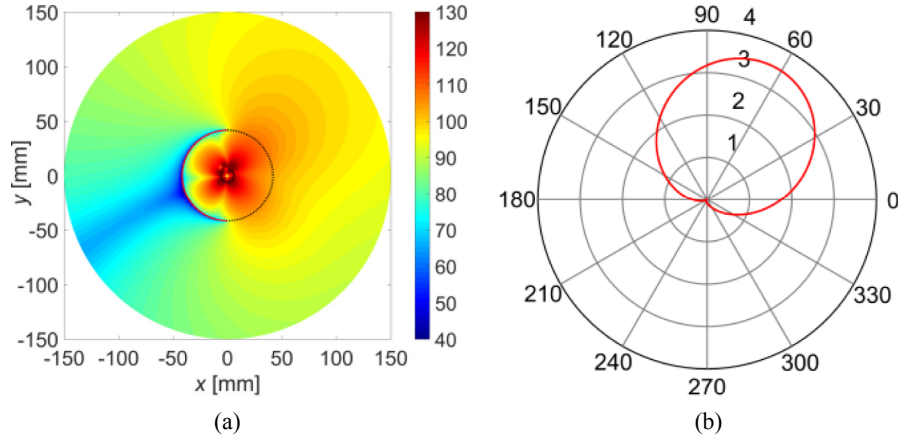
Fig. 9. The electric field magnitude (a) and the distinctive Huygens-like directivity pattern (b) for the optimized C2 configuration. The aperture extent is $2\theta = 180°$ and the outer shell radius is $b = 41.7$ mm. The minimum PR value is 36.64 dB and the maximum of the directivity pattern, 3.52 (=5.46 dB), occurs when $\varphi = 64.00°$.
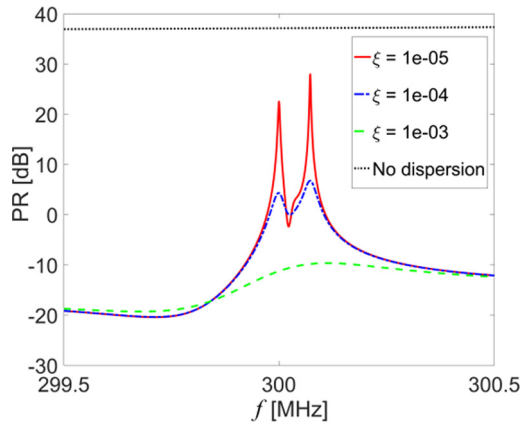

Fig. 10. The PR values as a function of the source frequency f for the optimized C2 configuration shown in Figure 7, but with the Lorentz model of the DNG core material. The parameter ξ represents the amount of loss included in the Lorentz dispersion model.

where $\zeta(\omega)$ denotes both the permittivity, $\varepsilon_2(\omega)$, and the permeability, $\mu_2(\omega)$, of the DNG core. The corresponding free-space parameters are denoted by ζ_0. The terms $\omega_{p\zeta}$, Γ_ζ, and $\omega_{r\zeta}$, denote, respectively, the plasma frequency, the collision frequency, and the resonance frequency of the model; these are of the electric type when $\zeta(\omega) = \varepsilon_2(\omega)$, and of the magnetic type when $\zeta(\omega) = \mu_2(\omega)$. Moreover, $\zeta'(\omega)$ denotes the real part of $\zeta(\omega)$, while $-\zeta''(\omega)$ denotes its imaginary part. For the latter, $\zeta''(\omega) = 0$ corresponds to the previously studied lossless case, whereas $\zeta''(\omega) > 0$ corresponds to a passive and lossy case of interest to the present section. The same Lorentz model was thus used for both material parameters of the DNG core. It was designed to recover the lossless DNG core permittivity and permeability values given in Table 1 for the C2 configuration when the angular frequency of operation, $\omega_0 = 2\pi f_0$, $f_0 = 300$ MHz. In particular, the plasma frequencies, $\omega_{p\zeta}$, used in (10) are obtained by requiring the real part of $\zeta(\omega)$ to recover the desired parameters $\varepsilon_2(\omega_0) = -\varepsilon_0$ and $\mu_2(\omega_0) = -\mu_0$ in the lossless case (i.e., with $\Gamma_\zeta = 0$). Moreover, both

electric and magnetic resonance frequencies were set to $\omega_{r\zeta} = 2\pi f_{r\zeta}$, $f_{r\zeta} = 295$ MHz. Note that the DNG core and the free-space shell have the same wave impedance as free space for all frequencies and for all loss values. To control the amount of loss in the material model, the collision frequency, Γ_ζ, was set to $\Gamma_\zeta = \xi\omega_0$, with the constant $\xi = 0$, 10^{-3}, 10^{-4}, and 10^{-5}. Thus, the DNG core cases were dispersive but lossless ($\xi = 0$), as well as dispersive and slightly lossy when $\xi > 0$. The effects of dispersion and losses on the performance of the C2 configuration are illustrated in Figures 10 and 11.

The PR values are shown in Figure 10 as a function of source frequency in the interval $f \in [299.5 - 300.5]$ MHz. The dispersionless and lossless case is included for comparison. It yields a constant PR value across this narrow range of frequencies. The inclusion of the dispersion significantly narrows the bandwidth of the resonance attained at 300 MHz. In addition, the presence of loss decreases the maximum PR value attained at 300 MHz. The decrease, of course, is smallest for the smallest loss case, i.e., for $\xi = 10^{-5}$. Furthermore, it is interesting to note that an additional resonance peak appears in Figure 10 just above 300 MHz. This resonance corresponds to a dipole mode inside the open PEC shell.

Consider the Lorentz model in the neighborhood of its resonance. One frequency at which the denominator goes to zero occurs slightly below 300 MHz in order for the model to produce the requisite negative number for both the real parts of the permittivity and permeability at 300 MHz. However, there is another frequency above and close to 300 MHz that produces nearly the same permittivity and permeability values. Thus, two resonances appear when the Lorentz model represents the DNG core material parameters. Because the second one is at a higher frequency, the dipole mode dominates the spectral behavior.

One sees immediately in Figure 10 that the peak PR values decrease significantly for all but extremely tiny losses, i.e., for the smallest ξ values. Thus, the corresponding electric near-field levels and directivity values are expected to decrease in magnitude as well. This is indeed
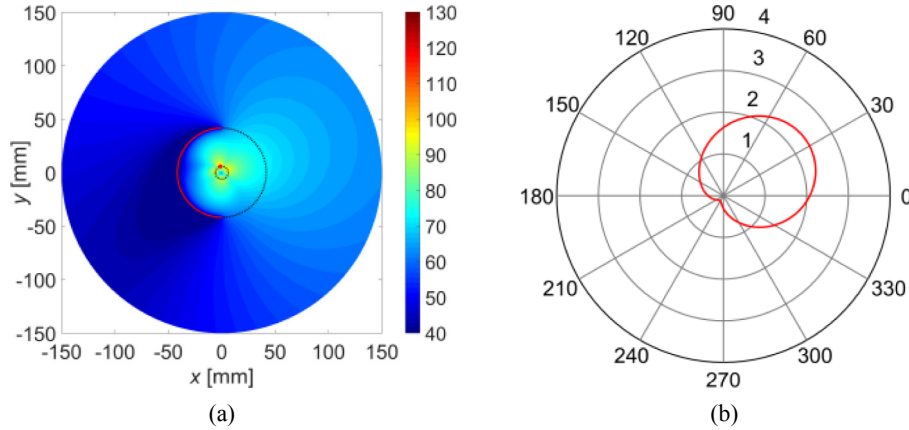
Fig. 11. The electric field (a) and the directivity (b) for the optimized configuration C2 at 300 MHz with its DNG core described by the Lorentz model whose loss component is very small, i.e., with $\xi = 10^{-4}$.

the case as demonstrated in Figure 11. The electric near-field magnitude, Figure 11a, and the directivity pattern, Figure 11b, are shown for $\xi = 10^{-4}$. In comparison to the lossless case shown in Figure 9, the peak values are lower. Nonetheless, note that the shape of the Huygens-like directivity pattern remains intact, but its peak value and direction have decreased to 2.39 ($=3.78$ dB) and $\varphi = 34.00°$.

Before finalizing the present section we note that the losses, which significantly affect the response of the C2 configuration, can be overcome by introducing gain into the structure. Moreover, once amplification of the resonant response occurs, significantly higher levels of radiated power are achievable in comparison to the lossless configurations. Detailed results on this issue are provided in Appendix B.

4 Summary and conclusions

We have reported an analytically-based investigation of the electromagnetic properties of a class of 2D asymmetric MTM-based open resonators excited by an ELS. These open resonators were composed of two infinite and concentric cylindrical layers covered with an infinitely thin PEC shell having an infinite axial slot whose angular extent was variable. By enforcing the boundary conditions, dual-series system of equations for the scattering coefficients were obtained. This system was transformed into an equivalent Riemann–Hilbert problem and solved analytically. The solution, which accounts for the presence of the edge singularities of the open PEC shell covering its layered MTM interior, converges well for a finite number of terms in the modal expansions.

A variety of performance characteristics follow immediately once the scattering coefficients of the scattered and incident fields are known. Particular attention was devoted to two types of interiors of the open PEC shells. One was composed of a DNG core and a free-space shell; the other was composed of a free-space core and either a DPS or DNG shell. Both open resonators were found to lead to large resonant enhancements of the power radiated by the line source for particular configurations. Notable differences between the performance characteristics of each were

presented and discussed. In particular, it was demonstrated that an electrically small open resonator could realize steerable Huygens-like directivity patterns with very high peak values. The impact of dispersion and losses, as well as gain introduction, was revealed by representing the DNG material properties with both a passive and active Lorentz model.

The presented asymmetric MTM-based open resonator designs may serve as potential candidates for a great variety of scientific and engineering applications in which enhanced directional responses in both the near- and far-field regions, along with notable beam shaping and steering capabilities, are desired. The consequent electrically small, directed transmitting and receiving antennas are an enabling, transformational technology for compact wireless power transfer, RFID, imaging, and sensor systems.

Nevertheless, it is important to note that the available present-day MTM unit-cells are still too bulky in size and shape to fit into and complete the MTM layers needed to realize the asymmetric resonators considered in this work. Consequently, the experimental verification of our structures is still beyond reach at the current stage of the MTM research in the microwave regime. Nonetheless, we expect that similar effects will be facilitated by SNG media, e.g., ENG instead of DNG metamaterials. Thus, the reported asymmetric resonators should be realizable at optical frequencies with naturally occurring plasmonic materials. Experimental testing of our designs thus awaits nanotechnology fabrication and optical measurements.

We note again that the analytical techniques reported in this paper were applied to a 2D cylindrical case with a single aperture in the PEC shell. They required the PEC shell to be infinitely thin. The method can readily be extended to cases having multiple apertures both in 2D cylindrical and 3D spherical [24] geometries. These canonical analytical problems are the subject of future research efforts. Another important research direction would be to examine numerically with, e.g., commercial software the influence of an open metallic shell with finite, and thus realistic, thickness on the resonant responses of these electrically small asymmetric open resonators. We have confidence in this numerical approach since the
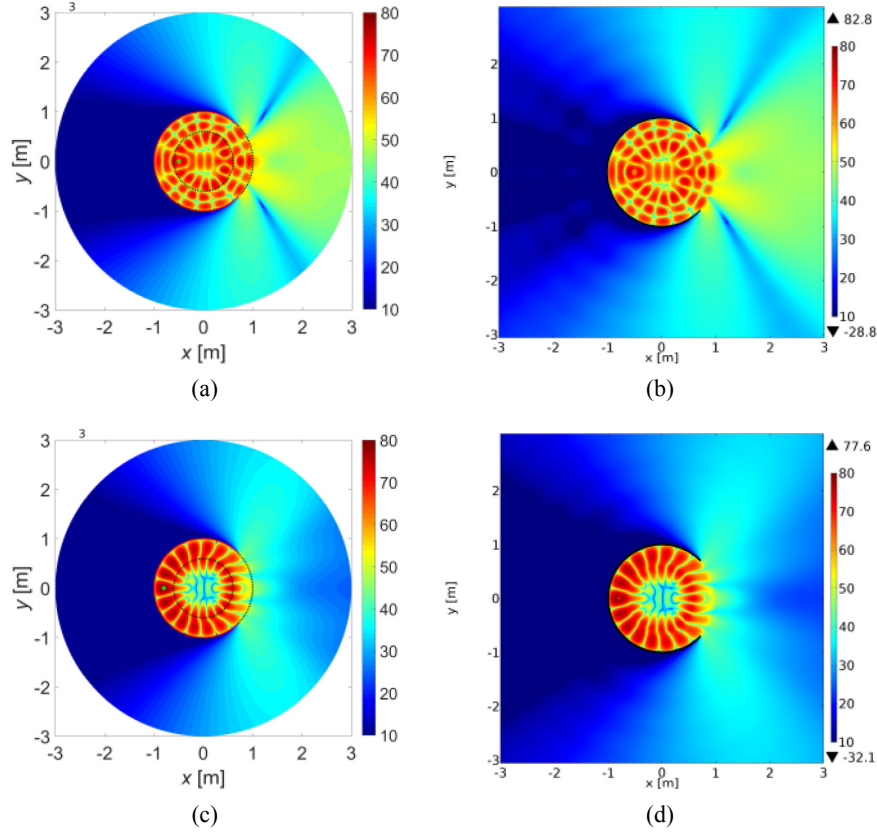
Fig. A.1. The analytically and numerically determined magnitudes of the electric field in dB, i.e., $20\log_{10}|\boldsymbol{E}/1[\text{V/m}]|$, for the validation configuration A: (a) and (b), and B: (c) and (d). The left column gives the analytical Matlab results. The right column gives the numerical COMSOL Multiphysics results.

comparisons we reported between our analytical and numerical results for the infinitesimally thin PEC shell were in such excellent agreement.

Appendix A

The analytical solution outlined in Section 2 was implemented in a Matlab code and was validated extensively through comparisons of these analytical results with the numerical results obtained in COMSOL Multiphysics, Version 5.0 [23]. Apart from the field distributions and far-field quantities, comparisons of the surface current density, $\boldsymbol{J}_s$, induced on the open PEC shell were emphasized. Because it is directed parallel to the edges of the aperture, this current density experiences a square root singular behavior at the edge. Consequently, it is a sensitive quantity that leads to accurate validations of the scattering coefficients. In particular, when the open resonators are excited with the ELS, the analytical expression for the surface current density takes the form of

$$\boldsymbol{J}_s = -\hat{z}\frac{jI_e k_0}{4}\Big(g_0\tau_0 - f(\varphi) + \sum_{m\neq 0}\frac{x_m\tau_m}{m}e^{jm\varphi}\Big) = \hat{z}J_z, \quad (\text{A.1})$$

where the various terms in it were defined in Section 2.

To illustrate the validation of the code representing the analytical solution, we discuss two representative configurations labeled as A and B. Their material and

geometrical parameters are summarized in Table A.1. The source frequency was selected to be 300 MHz and the quantity $\lambda_0 = 2\pi/k_0 = 1.0$ m is the corresponding free-space wavelength. For both configurations the aperture extent was set equal to $2\theta = 90°$.

Figure A.1 illustrates the magnitude of the near-field electric field distribution for configuration A: (a) and (b), and B: (c) and (d). For both configurations the ELS is located along the negative x-axis. For configuration A, the radial distance from the origin to the ELS is $\rho_s = 0.5\lambda_0$, while for configuration B it is $\rho_s = 0.8\lambda_0$. The left column of Figure A.1 shows the analytical results obtained in Matlab, while the right column shows the corresponding numerical results obtained with COMSOL Multiphysics. Very good agreement is found in all cases between the analytical and numerical results.

The very good agreement between the two methods is further demonstrated by the results in Figure A.2, which shows the surface current density determined analytically and numerically at the interface $\rho = b$ as a function of the observation angle φ for the configurations A (a) and B (b). For clarity, it is noted that the PEC shell extends over the angular region defined by the interval $\in[45°, 315°]$, i.e., the aperture extent is $2\theta = 90°$. At the edges of the PEC shell ($\varphi = 45°$ and $\varphi = 315°$), the surface current density exhibits the edge singularity behavior. There is a small discrepancy between the peaks of the analytical and numerical results at the edges of the aperture because of the discretization used for each. A finite number of expansion modes (the software
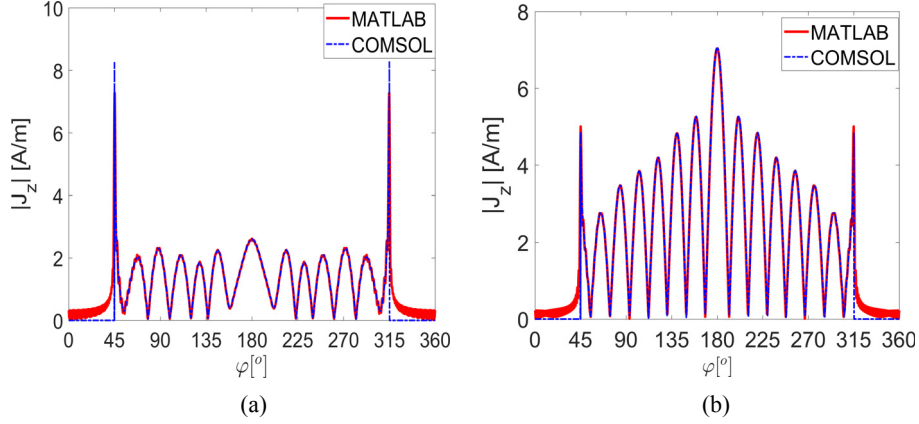
Fig. A.2. The surface current density, J_z, on the open PEC shell determined analytically (Matlab) and numerically (COMSOL Multiphysics) as a function of φ for the configuration A (a) and B (b). The PEC shell extends over the interval $\in [45°, 315°]$, i.e., having an aperture extent $2\theta = 90°$.
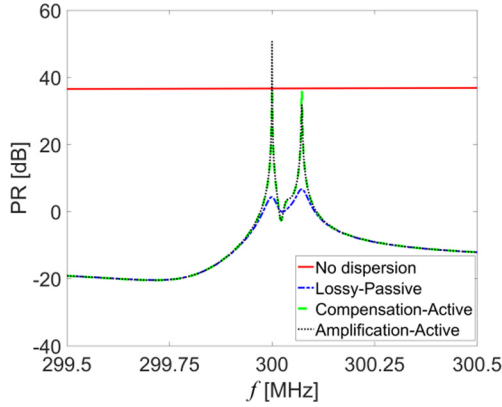

Fig. B.1. The PR values as a function of the source frequency f for the optimized C2 configuration where the gain-impregnated DNG core is modeled with a permittivity and permeability given by (11). This allows introduction of the gain needed to overcome the losses. See the main text for further explanations.

environment crashes if more than 150 are used for the validation configurations presented in this appendix) were used for the analytical results and the mesh resolution of the COMSOL Multiphysics results was finite, both being limited by the available computer memory. In theory, the magnitude of the surface current density is infinite immediately at the edges. It would require an infinite number of modes in the analytical solution to recover this behavior exactly and an infinitely fine mesh resolution with the numerical solution. The slight offset of the singular peaks away from the edges and a rounding-off of those peak values simply represent a spatial version of the Gibbs phenomenon. Nonetheless, it is quite clear from these comparison results that the analytical results are quite accurate. Moreover, they are immensely less time consuming to obtain.

Appendix B

In Section 3 it was noted that losses significantly affect the response of the C2 configuration. These losses can be fully overcome by introducing gain into the configuration. To

Table A.1. The material and geometrical parameters for the two validation problems.

C	ε_2	μ_2	ε_1	μ_1	a	b
A	ε_0	$10\mu_0$	ε_0	$10\lambda_0$	$0.6\lambda_0$	λ_0
B	$10\varepsilon_0$	μ_0	ε_0	$5\mu_0$	$0.6\lambda_0$	λ_0

illustrate this outcome, we introduce frequency-dependent gain inside its DNG core. In particular, the modified permittivity and permeability of the DNG core were taken to be

$$\zeta_A(\omega) = \zeta(\omega) + j\zeta_0 \frac{\omega_{p\zeta}^2 \Gamma_{\zeta,A}}{(\omega^2 - \omega_{r\zeta}^2)^2 + (\Gamma_{\zeta,A}\omega)^2}, \qquad (B.1)$$

with $\zeta(\omega)$ given by (10). The new term in (B.1) is associated with and has the same form as the loss term $\zeta''(\omega)$ in (10). In a similar manner, its collision frequency, $\Gamma_{\zeta,A}$, controls the amount of gain. For $\Gamma_{\zeta,A} = 0$, the model (B.1) recovers the passive model (10). On the other hand, when $\Gamma_{\zeta,A} = \Gamma_\zeta$, we exactly include the amount of gain needed to fully compensate for the losses. Finally, for a specific value of $\Gamma_{\zeta,A} > \Gamma_\zeta$, we attain an amplification of the response, i.e., the PR levels surpass those obtained in the lossless and nondispersive case reported in Figure 10.

An example is highlighted in Figure B.1 where the PR is shown as a function of frequency for the following four cases: lossless and nondispersive case (labeled as "No dispersion") obtained when $\Gamma_{\zeta,A} = \Gamma_\zeta = 0$; lossy and passive case ("Lossy-Passive") obtained when $\Gamma_\zeta = 0.0001\omega_0$ and $\Gamma_{\zeta,A} = 0$; active, loss-compensated case ("Compensation-Active") obtained when $\Gamma_{\zeta,A} = \Gamma_\zeta = 0.0001\omega_0$, and amplification case ("Amplification-Active") obtained when $\Gamma_\zeta = 1.034\Gamma_{\zeta,A}$. The first two were reported previously in Figure 10; they are included here for reference purposes. The peak PR value occurs at 300 MHz in the "Compensation-Active" case, which recovers, as expected, the PR value from the lossless and nondispersive case. When slightly more gain is included, one arrives at the

"Amplification-Active" case where the peak PR value gets amplified to a remarkable 50.63 dB. This result clearly confirms that gain impregnation of the DNG core can overcome the losses present in realistic DNG materials and a super-resonant state can be attained. Similar super-resonant states were reported in active plasmonic-based coated nano-particles at optical frequencies [6,25,26].

Note that the same amount of gain was included in both the permittivity and permeability of the DNG core in the active cases. Nevertheless, recalling that the infinite structure and its excitation by the infinite ELS represent a 2D TM configuration, the same results are obtained by including gain only in the permeability of the DNG core. Moreover, it is also important to note that any further increase of the amount of gain will detune the resonance and, hence, result in a drastic decrease of the PR values. Finally, we note that for the "Compensation-Active" case, the exact same near-field and directivity profiles are obtained as those in the nondispersive and lossless case reported in Figure 9. On the other hand, the response in the "Amplification-Active" case resembles the one reported in Figure 7. The dominant presence of the gain in the active core amplifies that modal distribution, which is associated with the structural configuration, rather than the rotated one in Figure 9, which arises from the rotated ELS position and the subsequent strong interaction of its field with the edge of the passive structure.

References

1. N. Engheta, R.W. Ziolkowski, IEEE Trans. Microw. Theory Tech. **53**, 1535 (2005)
2. A. Alù, N. Engheta, J. Appl. Phys. **97**, 094310 (2005)
3. S. Arslanagic, R.W. Ziolkowski, O. Breinbjerg, Radio Sci. **42**, RS6S15 (2007)
4. A. Alù, N. Engheta, IEEE Trans. Antennas Propag. **55**, 3027 (2007)
5. A. Alù, N. Engheta, J. Opt. A **10**, 093002 (2008)
6. J.A. Gordon, R.W. Ziolkowski, Opt. Express **15**, 2622 (2007)
7. S. Arslanagic, R.W. Ziolkowski, Adv. Electromagn. **1**, 57 (2012)
8. L. Novotny, B. Hecht, *Principles of nano-optics* (Cambridge University Press, Cambridge, UK, 2012)
9. M. Agio, A. Alu, *Optical antennas* (Cambridge University Press, New York, NY, USA, 2013)
10. A.E. Krasnok, C.R. Simovski, P.A. Belov, Y.S. Kivshar, Nanoscale **6**, 7354 (2014)
11. S.D. Campbell, R.W. Ziolkowski, IEEE J. Sel. Top. Quantum Electron. **21**, 312 (2015)
12. M.W. Knight, N.J. Halas, New J. Phys. **10**, 105006 (2008)
13. J.B. Lassiter, M.K. Knight, N.A. Mirin, N.J. Halas, Nano Lett. **9**, 4326 (2009)
14. F.D. Gakhov, *Boundary value problems* (Pergamon, London, 1966)
15. W.A. Johnson, R.W. Ziolkowski, Radio Sci. **19**, 275 (1984)
16. R.W. Ziolkowski, W.A. Johnson, K.F. Casey, Radio Sci. **19**, 1425 (1984)
17. R.W. Ziolkowski, J.B. Grant, IEEE Trans. Antennas Propag. **35**, 504 (1987)
18. R.W. Ziolkowski, J. Math. Anal. **16**, 358 (1985)
19. V.H. Koshparënok, V.P. Shestopalov, USSR Comput. Math. Phys. **11**, 222 (1971)
20. A. Nosich, V.P. Shestopalov, Radio Eng. Electron. Phys. **24**, 1949 (1979)
21. C.A. Balanis, *Advanced engineering electromagnetics* (John Wiley & Sons Inc., USA, 2012)
22. J.G. Van Bladel, *Singular electromagnetic fields and sources* (Clarendon Press, Oxford, 1991), Chapter 4.
23. COMSOL Multiphysics website [Online]. Available: https://www.comsol.com/, 2017
24. R.W. Ziolkowski, W.A. Johnson, J. Math. Phys. **28**, 1293 (1987)
25. S. Arslanagic, R.W. Ziolkowski, J. Opt. **12**, 024014 (2010)
26. S. Arslanagic, Y. Liu, R. Malureanu, R.W. Ziolkowski, Sensors **11**, 9109 (2011)